



UNIVERSITY OF LEEDS

This is a repository copy of *In Situ Melt Temperature Analysis During High Pressure Gas Atomization Of Liquid Metals*.

White Rose Research Online URL for this paper:

<https://eprints.whiterose.ac.uk/210957/>

Version: Accepted Version

Article:

Mullis, A.M. orcid.org/0000-0002-5215-9959 (2024) In Situ Melt Temperature Analysis During High Pressure Gas Atomization Of Liquid Metals. *Atomization and Sprays*, 34 (3). pp. 53-71. ISSN 1044-5110

<https://doi.org/10.1615/atomizspr.2024049993>

This is an author produced version of an article published in *Atomization and Sprays*. Uploaded in accordance with the publisher's self-archiving policy.

Reuse

Items deposited in White Rose Research Online are protected by copyright, with all rights reserved unless indicated otherwise. They may be downloaded and/or printed for private study, or other acts as permitted by national copyright laws. The publisher or other rights holders may allow further reproduction and re-use of the full text version. This is indicated by the licence information on the White Rose Research Online record for the item.

Takedown

If you consider content in White Rose Research Online to be in breach of UK law, please notify us by emailing eprints@whiterose.ac.uk including the URL of the record and the reason for the withdrawal request.



eprints@whiterose.ac.uk
<https://eprints.whiterose.ac.uk/>

1 ***In situ* Melt Temperature Analysis During High Pressure Gas Atomization**
2 **of Liquid Metals**

3
4 *A.M. Mullis**

5 University of Leeds, Leeds, LS2 9JT, UK.
6

7 ***Abstract***

8 We explore the extent to which imaging of the melt plume during High Pressure Gas
9 Atomisation using consumer DSLR (Digital Single Lens Reflex) equipment provides useful
10 information about the process. We show that the colour imaging and high spatial resolution
11 can be a useful adjunct to the more widely reported imaging using specialist high frame rate
12 cameras. With knowledge of the camera's colour response curves, the ratio of the signals in
13 the red, green and blue channels can be used to make spatially resolved temperature estimates
14 of the material within the melt plume. Moreover, by combining these temperature estimates,
15 which depend only upon intensity ratios, with the actual intensity of the optical signal we
16 propose it is possible to obtain estimates of the relative surface area of the melt within the
17 plume. This in turn can be related to the local melt fragmentation rate within the atomization
18 plume.
19

20 **Keywords:** High pressure gas atomization, DSLR imaging, powder metals, pyrometry.
21
22
23

* Corresponding author: a.m.mullis@leeds.ac.uk, +44 (0) 113 343 2568

24 **1 Introduction**

25 High Pressure Gas Atomization (HPGA) is one of a number of techniques for producing metal
26 powders direct from the melt, others include water, ultrasonic and centrifugal atomization.
27 However, it is HPGA that is currently receiving most attention due to its ability to produce the
28 fine, spherical and satellite free powders demanded by Additive Manufacture (AM), with AM
29 processes driving a near exponential increase in the demand for such powders. Despite this,
30 HPGA remains a relatively poorly understood process, with the complex interaction between
31 the melt stream and the supersonic gas jets used to disrupt the melt leading to instabilities on
32 various time scales (for instance, see the review by Anderson & Achelis, 2017).

33

34 One of the factors contributing to this lack of understanding of HPGA is a dearth of techniques
35 to study the atomization process *in situ*. Atomization is usually performed as a batch process
36 with the Particle Size Distribution (PSD) being characterised for the batch of material
37 produced, a procedure that does not have the fidelity to capture short timescale variations in
38 the process. A relatively small number of *in situ* investigations have been undertaken using
39 high frame rate video recording and these have significantly improved our understanding of
40 the process, particularly in relation to the unsteady nature of gas atomization. The first such
41 was by Ting *et al.* (2005) who used Discrete Fourier Transforms (DFT) to analyse high speed
42 video data of the gas atomization process, identifying a range of instabilities with frequencies
43 typically in the range 5-50 Hz, with the dominant instability having a frequency around 25 Hz.
44 They ascribed these instabilities to unsteady melt flow to the atomization nozzle, a
45 phenomenon termed melt pulsation. High speed imaging coupled with DFT analysis was also
46 used by Mullis *et al.* (2008), but now with the region of interest confined to a narrow window
47 just below the melt nozzle. They were able to confirm melt pulsation, with frequencies in the
48 range 25-50 Hz, and also found evidence that the melt spray cone actually consisted of 1 or

49 more fast rotating jets of melt (typical frequency ~ 300 Hz), a feature subsequently confirmed
50 (Mullis *et al.*, 2011) using Particle Image Velocimetry (PIV). Similar conclusions were reached
51 by Achelis *et al.* (2007), who observed that the melt cone in a pressure swirl atomizer
52 comprised a hollow cone of multiple melt filaments. More recently, Bigg & Mullis (2020) have
53 used a statistical object tracking method to construct spatially resolved maps of the melt
54 velocity within the spray cone from multiple frames extracted from a high speed video
55 recording.

56

57 Modelling studies have also been instrumental in elucidating the processes occurring during
58 HPGA and in filling the knowledge gaps left by a lack of *in situ* observational techniques. A
59 detailed Computational Fluid Dynamics (CFD) study by Ting & Anderson (2004) established
60 details of the gas flow-field just below the melt nozzle, with this wake region being described
61 as either open or closed, depending upon the gas pressure utilised. Here, a closed-wake is
62 terminated by a downstream Mach disk which tends to prevent gas escaping the wake region,
63 while no such Mach disk is observed for an open-wake. Both structures have also been
64 observed experimentally by Mates & Settles (2005) using Schlieren imaging, with the
65 transition between the open- and closed-wake states, both of which are stable in gas only flow,
66 leading to a dramatic change in the melt aspiration pressure experienced at the melt nozzle
67 (Ting *et al.*, 2002). A number of subsequent studies have picked up this idea of the open- to
68 closed-wake transition, for instance modifying the shape the atomizer geometry to affect a
69 reduction in the pressure above which closure of the wake is observed (Motaman *et al.* 2015).

70

71 While the flow behaviour in gas-only flow has been modelled by many authors, the difficulty
72 in modelling two-phase flow and droplet break-up means that this area has received much less
73 attention. However, with increasing computing power this has started to be addressed more in

74 recent years, with simulations that model the melt as both a continuous phase (the Euler-Euler
75 or E-E approach) or as a discrete phase (the Euler-Lagrange or E-L approach). The former has
76 been used by Zeoli *et al.*, (2012) using the volume of fluid (VOF) approach coupled with large
77 eddy simulation (LES) techniques, wherein they identify three modes in which the atomiser
78 may operate, which they term nozzle filming, mixed filming with pinch-off, and no-filming.
79 The coupled VOF-LES method has subsequently been adopted by Neumann *et al.* (2016) to
80 study the breakup of a free falling liquid steel jet, while Li & Fritsching (2017) have used the
81 VOF approach coupled with an Eulerian-Lagrangian approach to simulate the PSD of particles
82 formed during gas atomization. Recently, Arachchilage *et al.* (2019) have also used a similar
83 model to investigate the effect of gas pressure on particle size distribution. However, the E-L
84 approach has tended to be somewhat more computational tractability, which has allowed
85 droplet break-up, either by the development of Kelvin-Helmholtz instabilities (Thompson *et*
86 *al.*, 2016, Kaiser *et al.*, 2018) or via a wave break-up model (Xu *et al.*, 2020) to be incorporated
87 into the models, which can generally simulate much longer atomisation times than E-E type
88 models.

89

90 While the monitoring of HPGA using high-speed filming techniques has provided both useful
91 insights into the physical processes operating, and provided validation data for the types of
92 modelling studies described above, the use of such equipment during commercial production
93 is both expensive and intrusive. Consequently, alternative technologies need to be sought.
94 Mullis & Dunkley (2016a, 2016b) have demonstrated that the use of acoustic monitoring holds
95 promise, although more work is required in this area due to the complexity of relating the
96 acoustic signals to atomizer performance. In this paper we explore whether imaging using low
97 cost consumer DSLR (Digital Single Lens Reflex) systems has a role to play in the *in situ*
98 observation of gas atomization.

100 While DSLR cameras lack the high frame rate of specialist high speed video cameras, they
101 benefit from high resolution and colour imaging. Here we explore whether the additional
102 information provided by colour imaging, a feature not usually available in all but the most
103 expensive of high speed cameras, can provide useful insights into the HPGA process. In
104 particular, we explore whether the colour information in DSLR images can be used for
105 temperature estimation within the melt plume and whether this can in turn be used to infer the
106 extent of melt break-up in different regions of the plume. The trade-off is the much reduced
107 temporal resolution of the DSLR system, with a typical frame repeat rate of 60 fps, compared
108 to the many thousands of frames per second obtained utilising a high speed camera.

109

110 The cost and resolution benefits of using DSLR equipment for temperature measurements have
111 been recognised by a number of previous authors (e.g. Jimenez 2020). Applications include
112 determination of sky quality (Fiorentin *et al.* 2020) and flame temperatures (e.g. Kuhn *et al.*
113 2011; Aphale & Desjardin, 2019; Sankaranarayanan *et al.* 2021 – with Table II in this last
114 article giving a more extensive list of such experiments), with this being applied to industrial
115 incineration processes by Zhou *et al.* (2022). The accuracy of this approach depends upon a
116 number of camera parameters, most notably ISO setting and shutter speed, with Zhou *et al.*
117 (2022) reporting mean squared errors between 20-95 K², based on a 60 ton incinerator with a
118 maximum flame temperature of 1510 K.

119

120 As discussed above, the DSLR frame rate is comparable to the typical frequencies of the melt
121 flow instabilities inherent in HPGA systems. In contrast to the melt, the high pressure gas flow
122 is generally considered to be highly stable, reflecting the fact that the melt embodies < 1% of
123 the momentum of the gas and 0.02% of the kinetic energy (see Bigg & Mullis, 2020, based

124 upon a gas velocity calculated via isentropic flow theory of Mach 2.8 and an RMS melt velocity
125 of 12.8 m s^{-1} , giving Reynolds numbers for the gas and melt of 63,000 and 3,900 respectively).
126 Consequently, while it is likely that such instabilities will be randomly sampled by the DSLR
127 system, tracking the temporal evolution of individual instabilities remains the preserve of true
128 high speed filming.

129

130 **2 Experimental Methods**

131 2.1 Atomization & Imaging Setup

132 Atomization trials were conducted using a commercial gas atomizer of the annular slit type
133 operating at a gas manifold pressure of 2.4 MPa. The melt nozzle is of the conventional
134 truncated cone type, with a flat 9 mm tip and a 30° apex angle. The central melt feed tube is 5
135 mm in diameter, with the liquid metal being drawn into the atomizer under gravity and by the
136 normal aspiration tendency of this atomizer design, wherein the time-averaged melt feed rate
137 is approximately 0.25 kg s^{-1} , with the gas flow rate being 0.35 kg s^{-1} . The total atomizing time
138 for a typical 200 kg batch is therefore 15-20 minutes. The melt being processed in the case
139 reported here is 316L stainless steel which is subject to a 200 K superheat, wherein the pour
140 temperature is $\sim 1900 \text{ K}$.

141

142 Imaging of the melt plume was by means of a standard consumer Nikon full-frame (i.e. 35 mm
143 charge-coupled device (CCD)) DSLR camera fitted with a Micro Nikkor 70-180 mm (f/4.5-
144 5.6D) lens. The frame size is 1920×1080 pixels at a frame rate of 60 fps with a shutter speed
145 during filming of $1/10000 \text{ s}$. A total of 414 frames were recorded over a filming interval of \sim
146 7 s. As shown schematically in **Figure 1**, the camera was positioned at the atomizer's viewport
147 with a working distance of around 45 cm and looking slightly upwards towards the melt plume,
148 the camera inclination from the horizontal being $\sim 20^\circ$. This was necessary as, unfortunately,

149 the atomizer was not equipped with a viewport directly in line with the melt plume. A typical
150 frame, extracted from the movie, is shown in **Figure 2**, with some extraneous background
151 having been cropped out of the image. Once this is done, the final image size is 469×775
152 pixels, giving a spatial resolution with the camera as setup above of 0.88 mm/pixel. Due to the
153 low temporal sampling rate when using a DSLR camera, the shape of the melt plume varies
154 considerably between frames. However, as shown by Mullis *et al.* (2017), using high speed
155 filming, the average plume shape (shown inset in Figure 1, in this case averaged over 28665
156 frame) is approximately cylindrical, but somewhat pinched in at the location of the expansion
157 waves of the supersonic gas. Given this is the same atomizer as studied here and operating
158 under very similar conditions, we consider that this is a good representation of the time-
159 averaged plume shape, albeit this is not evident from the DSLR images (although equally, the
160 average plume shape is not evident from the individual high speed camera frames from which
161 it was generated).

162

163 2.2 Image Analysis Methods

164 Pyrometry, both single colour and two colour, is a well-established temperature metrology
165 technique, with such systems generally using a very narrow part of the spectrum (see e.g.
166 Jimenez, 2020 for an overview of two colour pyrometry). In contrast, the DSLR has a much
167 wider spectral response designed to mimic the human eye. As such, the proposition here is
168 much closer to developing a DSLR equivalent of the conventional semi-quantitative foundry
169 technique of using a colour chart to gauge temperature. This will, of necessity, not have the
170 temperature accuracy of a dedicated pyrometry system, but the trade-off is the low cost and
171 high spatial resolution (1920 x 1080) characteristic of modern DSLR systems. A further
172 advantage of consumer DSLR equipment is that it is relatively easy to obtain data on the
173 spectral response of the CCD imaging detector from the numerous hobbyist magazines serving

174 this market. **Figure 3** shows the spectral response functions, R_R , R_G and R_B , for the red, green
 175 and blue channels respectively for camera used to obtain **Figure 2**. As only the ratios of these
 176 will be utilised they have been normalised such that the peak of the highest curve is equal to 1.
 177

178 Also shown in the figure is the spectral power, S_λ , as a function of wavelength, λ , for that part
 179 of the blackbody spectrum that falls within the optical response range, 350-700 nm and for two
 180 example temperatures likely to be present within the melt plume, namely $T = 1750$ K and $T =$
 181 1500 K. These curves are given by Planck's law:

182

$$S_\lambda(\lambda, T) = \frac{2hc^2}{\lambda^5} \left(\frac{1}{\exp\{hc / \lambda k_B T\} - 1} \right) \quad (1)$$

183

184 where h is Planck's constant, c is the speed of light and k_B is Boltzmann's constant. We now
 185 define the power function, $B_{\lambda,i}(\lambda, T)$, ($i = R, G, B$) for the R, G and B channels respectively by:

186

$$B_{\lambda,i}(\lambda, T) = S_\lambda(\lambda, T) \times R_i(\lambda) \quad (2)$$

187

188 where $R_i(\lambda)$, ($i = R, G, B$) is the spectral response function as plotted in **Figure 3**. The function
 189 $B_{\lambda,i}(\lambda, T)$, evaluated at the two temperatures shown in **Figure 3**, namely $T = 1500$ K and $T =$
 190 1750 K, is given in **Figure 4**. Note that the scales differ by one order of magnitude for $T =$
 191 1500 K and $T = 1750$ K. The response (0-255) of each channel within a pixel will then be
 192 proportional to integral, I_i , over wavelength, of the power function, $B_{\lambda,i}$, for the light falling on
 193 that pixel, where:

194

$$I_i(T) = \int_{350 \text{ nm}}^{700 \text{ nm}} B_{\lambda,i}(\lambda, T) d\lambda \quad (3)$$

195

196 From Equ. (3) we can estimate the relative response of the R, G and B channels in response to
 197 illumination by blackbody radiation of a given temperature. For instance, at the example
 198 temperatures used in **Figure 4**, the ratio I_R/I_G is 2.555 at $T = 1500$ K and 1.997 at $T = 1750$ K.
 199 Moreover, as we are using only a ratio of the power in different channels, we do not need to
 200 consider factors such as the emissivity of the sample or the aperture of the optics used, these
 201 being, at least to a first approximation, independent of wavelength.

202

203 From the above we can see that we can, in principle, use the ratio of the power in the R, G and
 204 B channels to estimate temperature based on colour. With three available channels we have
 205 two unique ratios, which we take as I_R/I_G and I_G/I_B , with the evaluation being subject to the
 206 condition that both the numerator and denominator are > 10 . For black areas where both the
 207 numerator and denominator of a ratio is 0, this is marked as NaN (not a number), which
 208 prevents these pixels appearing in any of the contour maps. However, as discussed in more
 209 detail below, this generally means that only one or other of the ratios is available for any given
 210 pixel. By performing the calculation described above for a wide range of temperatures we can
 211 build up a ‘look-up table’ of pixel RGB ratios to equivalent blackbody colour temperatures,
 212 this being shown graphically in **Figure 5**. In this calculation we use a temperature range of 600
 213 K – 3200 K, with increments of 2 K. Applying this to an image, such as that shown in **Figure**
 214 **2**, we therefore have the basis for obtaining a spatially resolved map of the temperature within
 215 a high pressure gas atomisation plume.

216

217 It may be imagined that there is a two-fold redundancy in the temperature determination with
 218 both the I_R/I_G and I_G/I_B ratios being used at each pixel. Unfortunately, this is not the case due

219 to the large difference between I_R and I_B . If the image in **Figure 2** is exposed such that no pixels
220 have any channel (R, G or B) saturated, the intensity recorded in the B-channel is, for the
221 majority of the pixels, so low (< 10 on 0-255 scale) that significant discretisation errors will
222 occur. Conversely, increasing the image exposure leads to significant numbers of pixels in the
223 R-channel being saturated. The best compromise appears to be to expose so as to get a good
224 dynamic range, without saturation, in the G-channel. In the brighter areas of the image this
225 leads to pixels which are saturated in the R-channel, but a good temperature determination can
226 be made from I_G/I_B . Conversely, in the darker areas of the image the signal in the B-channel is
227 < 10 (0-255 scale), but a good temperature determination can be made from I_R/I_G .
228 In fact, only 0.4% of pixels (8800 out of 1920x1080) fall within the exposure range where both
229 the I_R/I_G and I_G/I_B ratios can be used to make a temperature determination, although these give
230 temperatures which map well onto each other. Moreover, the final results may be sanity
231 checked against the experimental conditions, wherein temperatures close to the pour
232 temperature are expected close to the nozzle.

233

234 So far, we have demonstrated that by using the ratio of the channel intensities, I_R/I_G and I_G/I_B
235 that we can make an estimate of the melt plume temperature. However, with reference to the
236 standard Stefan-Boltzmann law for the total power, P , emitted by a body of surface area A with
237 emissivity ε :

238

$$P = \varepsilon \sigma A T^4 \quad (4)$$

239

240 it is clear that with knowledge of both the temperature of the radiating body and the absolute
241 intensity of the emission, it is possible to also deduce the area of the emitting body (here σ is
242 the Stefan Boltzmann constant), wherein the degree to which the melt is being locally

243 fragmented may be estimated. Of course, when using a DSLR camera we have to take into
244 account a number of other factors as well. The first of these is that the image of the droplet is
245 projected onto the flat imaging plane of the CCD, wherein we detected the apparent area of the
246 projection, rather than the true area of the population of 3D droplets. The second factor is that
247 we also have to take account of the spectral response of the CCD. To address the second factor,
248 rather than using the total radiant flux as expressed by Equ. (4), we consider the absolute
249 intensity of one of the channels, in this case I_G . As explained above, for the exposure model
250 adopted here, the green channel is a better choice than either red, which is frequently saturated
251 in the high intensity areas of the image, or blue which generally suffers from low intensity in
252 large areas of the image. Specifically, with the temperature now given at each pixel within the
253 image we use Equ. (3) to estimate the intensity of the signal in the green channel, I'_G , for *unit*
254 *emitting area*. The ratio of I'_G to the actual response of the pixel, I_G , will then give a *relative*
255 *measure of the radiating area contained within that pixel*. That is, contouring the ratio I_G / I'_G
256 will give a measure of the *relative surface area* of the melt at each pixel, which in turn is related
257 to the particle size distribution within that pixel and consequently the extent of melt
258 fragmentation. As we are not able to directly calibrate the system, that is we do not know the
259 size, and hence surface area, of the droplets contributing to the emission from any given pixel,
260 we restrict the analysis given here to an estimation of *relative surface area* within the plume
261 wherein, we do not need to be concerned with the mapping between apparent surface area in
262 the imaging plane to true surface area of the particles, as this is accounted for in the relative
263 scaling, as is the $\varepsilon < 1$ for the melt (i.e. the approach is valid for grey, not just black bodies).
264 This *relative surface area* will be a function primarily of the particle size distribution within a
265 particular pixel, with finer particles giving a higher apparent surface area. To a lesser extent it
266 will also reflect the volume of melt being imaged within that pixel, although given the almost
267 cylindrical nature observed for the melt cone (see Figure 1 below) we believe this is likely to

268 be a secondary effect. Consequently, the technique gives a mechanism to image where the gas
269 is interacting most strongly with the melt within the plume and where the local fragmentation
270 rate is highest.

271

272 Implicit within this approach is the assumption that the emissivity of the melt within the plume
273 is constant. Over a limited temperature range (~ 200 K) this has been shown to be approximately
274 true for various steels (Larciprete *et al.*, 2017), while over a larger temperature range (> 1000
275 K) a number of transition metals have been shown to display a modest increase in emissivity
276 with increasing temperature (Sievers, 1979). However, in most cases surface condition (degree
277 of oxidation, cleanliness etc.) has been shown to be a much more significant influence.
278 Consequently, given the dearth of reliable measurements of metal emissivity as a function of
279 temperature, and the variability therein (see e.g. Figure 1 in Felice & Nash, 2013), we believe
280 that the assumption of constant emissivity is likely to be no worse than attempting to correct
281 for any potential variation in emissivity.

282

283 2.3 Frame Selection & Error Estimation

284 In order to establish which frames within the movie to analyse in detail we have used the
285 technique suggest Mullis *et al.* (2008) in which the average brightness of the material passing
286 through a narrow window just below the melt nozzle is assessed. The method is given in detail
287 by Mullis *et al.* so is not reproduced here, the only deviation from their procedure being that
288 we average across all three colour channels. The sampling window used is 5 pixels high and is
289 located 50 pixels below the point at which bright melt is first observed at the top of the frame,
290 with this being shown schematically in **Figure 2**. This value is chosen so as to ensure the
291 sampling window is fully clear of the melt outlet, which due to the camera orientation is
292 observed as an elliptical orifice, the back edge of which is lower in the image than the edge

293 closest to the camera. The back edge of the melt outlet is not visible in all frames, but where it
294 is, this positioning corresponds to the sampling window being 5 pixels below the lowest point
295 of the back edge of the outlet. This also locates the sampling window in the “neck” of the melt
296 plume. i.e. the region where the plume is at its narrowest and is not yet strongly interacting
297 with the supersonic gas. As such, to a good approximation, the melt is subject to negligible
298 fragmentation, wherein the melt brightness within this window may be used as a proxy for the
299 volume of melt instantaneously at the melt nozzle. Moreover, as the melt nozzle itself is heated
300 (to prevent freezing of the melt in the initially cold ceramic) there is also only marginal cooling
301 of the melt below the pour temperature at this location, wherein the accuracy of the optical
302 temperature determination using the above method can be checked against that of a
303 thermocouple sitting just above the nozzle inlet. For the image shown in Figure 2, the average
304 optically determined temperature within the indicated sampling window is 1862 K (with a
305 variation of ± 2 K within the sampling window), which compares with a contemporaneous
306 thermocouple reading of 1915 K. However, as we are unable to calibrate at other points within
307 the melt plume, we consider that a typical temperature error of 10% might be realistic. Given
308 the 4th power dependence of radiant power (& therefore in our calculation apparent surface
309 area) upon temperature, this would equate to a 40% error in surface area due to errors in
310 temperature determination. An overall error of a factor of 2 in area might therefore be in order.

311

312 **3 Results**

313 A temperature map, corresponding to the image shown in **Figure 2**, is given in **Figure 6a**. This
314 is, as far as we are aware, the first time a spatially resolved temperature map of a gas
315 atomisation plume has been obtained. The results appear reasonable with the brightest areas in
316 **Figure 2** appearing as the hottest in the temperature map (note that only ratios of intensities in
317 the RGB channels were used to determine the temperatures, not absolute intensities) and with

318 temperatures that seem consistent with the experiment performed, that is with a maximum close
319 to the pour temperature of ~ 1900 K, dropping to around 1000 K at the limit of detection.
320 Although, for the sake of brevity not shown, we have also calculated numerically ∇T from the
321 temperature values in the map in order to assess the extent to which we may take the
322 temperature as being uniform with a given pixel, with the magnitude of ∇T varying from
323 around 2.5 K per pixel in the centre of the hot plume (see position A in **Figure 6a** as being
324 typical) to ~ 150 K per pixel at the margins of the hottest material within the central plume (see
325 position B in **Figure 6a** as being typical). Where these large temperature gradients exist, albeit
326 this being a relatively small area fraction of the total image, it must be remembered that the
327 indicate temperature is an average for the pixel and local variation will occur.

328

329 We note that large areas in the interior of the plume have undergone little cooling which
330 suggests melt in these regions are experiencing only minimal fragmentation due to interaction
331 with the high velocity gas, or that heat transfer is limited as the surrounding gas is in thermal
332 equilibrium with the melt. Conversely, material on the margins of the plume appear much
333 cooler, suggesting that significant fragmentation is restricted to this region, with the resulting
334 smaller droplets losing heat more rapidly. This is borne out by the map of *relative melt*
335 *projection area* given in **Figure 6b**. Each pixel will contain a range of melt particle sizes,
336 together with melt ligaments and more complex structures indicative of break-up, such as
337 sheets and bags (see e.g. Hsaing and Faeth, 1992). These will have a characteristic projection
338 area on the imaging plane of the camera, which is the measure being determined here.
339 Generally, we would expect finer features (i.e. regions where the melt is interacting most
340 strongly with the high velocity gas) to display the largest *relative melt projection area*.

341

342 We note that the regions of the plume with the highest and lowest *relative melt projection area*
343 differ by around a factor of 10^5 (despite a scale that runs from 0 to 255 on the green channel
344 used for this determination). Such a large variation in apparent surface area is permitted in the
345 mapping due to the T^4 dependence of P , i.e. a low temperature high P reading maps onto a
346 much larger value of A than a high temperature low P reading, with this range spanning five
347 orders of magnitude).

348

349 As described above, we use the brightness in narrow window just below the melt delivery to
350 identify key frames to study. As the melt has not interacted strongly with the gas at this point,
351 it will have experienced little cooling or fragmentation. The resulting time-series may thus be
352 regarded as an indicative melt flow rate of the material at the nozzle for each frame, and is
353 given in **Figure 7**. A number of features are evident from the plot including a high frequency
354 variation in intensity which is not fully resolved by the 60 fps imaging and a long period
355 oscillation with a period comparable to the total filming time of ~ 7 seconds. There is also an
356 extreme low intensity excursion (frame 97, shown in more detail in the insert to **Figure 7**) in
357 which the intensity drops to 36.9 (0-255 scale), less than half of its mean value of 85.5. We
358 also note a second, relatively extreme excursion in Frame 350 in which the mean intensity
359 drops to 56.4. The mean grey level within the sampling period is 85.53 and if this is associated
360 with the time average melt flow of 0.25 kg s^{-1} (and on the reasonable assumption of constant
361 gas flow, measures at 0.35 kg s^{-1}) the instantaneous gas to metal ratio would vary from 1.007
362 (frame 44, window mean grey level 118.83) to 3.246 (frame 97, window mean grey level 36.89)
363 compared to its time average value of 1.4.

364

365 Based on the data shown in **Figure 7**, we have selected the following frames for further
366 investigation, both to illustrate the applicability of the technique and to elucidate the

367 instabilities present within the gas atomization technique. As being representative of the normal
368 functioning of the atomizer we have selected frame 44 which has the highest recorded intensity
369 of 118.8, frame 243 which has one of the lower recoded intensities (excluding the extreme
370 excursions discussed above) at 68.5 and frame 269 which has an intensity of 85.3, close to the
371 global mean value. We also explore in more detail the extreme excursion observed in frame
372 97, examining this and the frames immediately before and after.

373

374 The set of images corresponding to the ‘normal’ operation of the atomizer (frame numbers 44,
375 243 and 269) is shown in **Figure 8**, with the corresponding temperature and *relative melt*
376 *projection area* maps being given in **Figures 9 & 10** respectively. Note that in **Figure 9**, an
377 artefact is visible in the top third of frames (a) and (c), with this being indicated with two black
378 elliptical outlines in part (a). This is due to the bright melt plume being reflected off the steel
379 gas delivery manifold, which can be seen illuminated as a dull red ring in **Figure 8**, labelled
380 with the word “Manifold” in part (a) of the figure. This artefact is due to the upward inclination
381 of the camera towards the melt plume and could be eliminated if the camera could be aligned
382 horizontally with the melt plume. With reference to **Figures 9 & 10** it is clear that the main
383 difference between periods of low flow (parts b) and other times (parts a & c) is that much less
384 of the interior of the plume is occupied by the hot melt that has minimal interaction with the
385 high speed gas stream. Nonetheless, the coolest material, which is therefore interacting most
386 strongly with the high speed gas, is confined to outer margins of the atomization plume.

387

388 The set of images centred around the low intensity excursion in frame 97 is shown in **Figure**
389 **11**, with the corresponding temperature and *relative melt projection area* maps given in
390 **Figures 12 & 13** respectively. From these figures the extreme nature of this event is apparent.
391 Specifically, in frame 96 (**Figure 11a**) although there is a strong outflow of bright melt from

392 the nozzle, the spatial extent of the melt plume is shorter than in any of the parts of **Figure 8**.
393 This is despite the mean intensity of the near nozzle region for frame 96 being 84.2, close to
394 the mean value over the filming period. Following this there is an almost complete shut-down
395 in the flow of melt in frame 97 (**Figure 11b**) with little evidence of bright melt in the image.
396 This is reflected in the corresponding temperature map (**Figure 12b**) in which the peak
397 temperature inside the plume is now 300-400 K below the pour temperature. The corresponding
398 *relative melt projection area* map (**Figure 13b**) shows that the low projection area melt, which
399 we would conjecture is essentially coarse and unfragmented, which is ubiquitous in the centre
400 of the melt plume in the other frames, is absent here. Finally, in frame 98 (**Figure 11c**)
401 significant bright melt is once again apparent within the melt plume, although the geometry
402 adopted is rather different from that observed in the other frames. Indeed, the morphology of
403 the melt plume is similar to that observed during membrane break-up, which is sometimes
404 observed at the beginning of atomization (Anderson 2011). This would be consistent with the
405 almost complete shut-down of melt flow in frame 97 and its restarting in frame 98. The
406 corresponding temperature (**Figure 12c**) and area (**Figure 13c**) maps show that this bright sheet
407 of melt is close to the pour temperature and with low *relative melt projection area* likely
408 remains largely intact during its first 50-60 mm of transit after being discharged from the melt
409 nozzle.

410

411 **4 Discussion**

412 With reference to **Figure 6b** we observe that the centre of the plume is dominated by melt with
413 low *relative projection area* that interacts only weakly with the supersonic gas, with the higher
414 area material being confined to the margins of the plume. The inference would be that the
415 interior of the melt plume is likely quite coarse, unfragmented melt, with the highest melt
416 fragmentation rate occurring only on the plume margins where there is a much higher shear

417 being generated. In this respect the results agree well with those found by Bigg & Mullis
418 (2020), in which high frame rate (16,000 fps) imaging was used to produce spatially resolved
419 maps of the velocity of the material in the melt plume *for the same atomizer* as studied here.
420 They found a strong interaction between the gas and the melt on the margins of the melt plume,
421 with the fastest moving material contained within a relatively narrow shell at the plume
422 margins. Conversely, in the centre of the melt plume they determined that the average velocities
423 were less than 10% of those recorded on the plume margins. In particular, they identified a
424 recirculation zone extending some 35 mm (~ 4 nozzle diameters) downstream of the melt outlet
425 in which the average melt velocity was ≈ 0 , indicating that the melt was just as likely to be
426 moving upwards towards the melt nozzle as away from it. In this recirculation zone shear would
427 be expected to be low and significant breakup of the melt would not be encountered. Likewise,
428 in this region extending ~ 35 mm downstream immediately below the melt nozzle outlet we
429 observe low surface area, likely corresponding to coarse particles and filaments of melt. We
430 speculate that this relatively narrow zone in which the melt interacts strongly with the fast
431 moving gas is one of the main causes of the notoriously low efficiency of HPGA processes in
432 utilising the considerable kinetic energy embodied in the supersonic gas jet to fragment the
433 melt stream.

434

435 We note by comparing the two parts of **Figure 6** that there is a very close correspondence
436 between the temperature and *relative melt projection area* maps, with high temperature being
437 associated with low surface area and *vice versa*. Given the field of view which extends only 60
438 mm or so downstream of the nozzle we believe this is inevitable, with the extent to which the
439 melt is fragmented dictating the subsequent cooling rate. That is, the temperature of the melt
440 in this near plume region is determined almost exclusively by the extent of breakup and hence
441 the area it present through which it may lose heat. We note that on the margins of the plume,

442 unlike location B in **Figure 6a**, the temperature gradient is typically quite small (< 10 K per
443 pixel), wherein the variation in temperature across the pixel is negligible relative to the average
444 temperature of the pixel (~ 1000 - 1200 K), i.e. heat is being lost at a uniform rate across layers
445 of width equivalent to the pixel resolution (0.88 mm).

446

447 It is widely recognized (see e.g. Li & Fritsching, 2017) that the final PSD in gas atomization is
448 established during secondary break-up (i.e. the break-up of droplets into smaller droplets). In
449 the analysis presented here, considering that the melt plume appears to be visible along its
450 whole length, we believe we are capturing both primary and secondary atomization (primary
451 atomization being the break-up of sheets and ligaments into particles), although as individual
452 melt droplets are not resolved it is not possible to distinguish these two processes within this
453 analysis.

454

455 The distribution *relative melt projection area*, as extracted from **Figure 6b**, is shown in
456 **Figure 14**. We conjecture that a pixel presenting a high surface area will contain a large number
457 of small particles, whereas one presenting a low surface area will contain a much smaller
458 number of large particles. As such, the histogram in **Figure 14** is a pixel count, contains
459 information about the particle size distribution (by pixel), but is not itself such a size
460 distribution. Moreover, the results may also be skewed by the viewing geometry. Specifically,
461 viewing its projection area may lead to an underestimate of the volume of the interior of the
462 melt cone, where the melt is least fragmented leading to the fraction of low area pixels being
463 underestimated. Conversely, we can see from the left- and right-hand margins of the plume (as
464 imaged in e.g. **Figure 2**) that the melt cone is bounded by a thin, cool layer which present a
465 much higher melt projection area. Given the approximate rotational symmetry of the melt cone
466 it is very likely such a layer exists in front of (and behind) the main body of the melt cone, but

467 is obscured by the much hotter, brighter interior of the melt cone. On balance, we suspect the
468 former effect is dominant over the latter. In some previous works (e.g. Aphale & Desjardin,
469 2019), multiple cameras have been used to correct for this viewing geometry effect, although
470 in our case this is not possible as the atomizer has only one viewport from which the melt plume
471 is visible. For similar reasons it was not possible to view the melt plume head-on, nor was it
472 possible to apply a perspective correction for this. To do so would have required modifications
473 that would have taken a commercial atomizer out of production for an extended period while
474 additional viewports were fitted,

475

476 We have also attempted to correlate the data in the histogram with the corresponding
477 temperature map (**Figure 6a**) to estimate the number of pixels that contain solid material, and
478 those that still contain melt and may therefore be undergoing further fragmentation. However,
479 here there is a further complication in that particles in free flight (i.e. melt in the absence on a
480 container) may undergo significant undercooling below the liquidus temperature before
481 solidification is nucleated, potentially by some 100's of Kelvin for the smallest particles (see
482 e.g. Mullis *et al.* 2020). In Figure 14 we have indicated where the split between solid particles
483 and melt droplets would occur if the onset of solidification occurred at the liquidus temperature,
484 and also given an indication of how this would be shifted if the average undercooling at
485 nucleation were 75 K or 150 K. From this it is clear that melt temperature and projection area
486 on the imaging plane are very closely correlated, the most natural explanation for this being
487 that the degree of melt fragmentation is the primary determinant of the melt temperature.

488

489 Factor in the rather large errors associated with the current method and the fact that in the
490 DLSR image fragmentation of the visible melt is incomplete (i.e. some material is fragmented
491 and solid, some is still liquid and continuing to undergo fragmentation), we would assert that

492 we have a technique that could be used to evaluate where within the melt plume significant
493 interaction with the high speed gas is occurring, and by inference to compare this between
494 atomizer designs, but that quantitative *in situ* determination of the particle size distribution
495 during atomization would require a much more sophisticated analysis.

496

497 The variability of the atomization process, as revealed by **Figure 7**, is consistent with that
498 found by Mullis *et al.* (2008), albeit for an atomizer of different scale (10 kg melt batch, 5 mm
499 nozzle) and design (18 discrete jets with 45° apex angle). That fluctuations in the melt flow of
500 the same order are observed in two HPGA systems of such widely different designs is
501 indicative of the ubiquitous nature of melt pulsation during gas atomization and also reflects
502 on the lack of success that atomizer equipment manufacturers have had in eliminating this
503 issue. As the gas flow will be constant, such fluctuations in the melt flow rate lead to significant
504 short term variations in the instantaneous Gas-to-Metal Ratio (GMR). Based on the strong
505 correlation between measured PSD and time-averaged GMR it has been speculated in the
506 literature that melt pulsation leads to short time-scale variations in the PSD of the powder being
507 produced (Mullis *et al.*, 2013), although there was no direct evidence of this. However, **Figure**
508 **13** shows now in more detail the effect upon atomization of a low melt flow excursion. Broadly,
509 as can be seen from **Figure 13b**, the material displaying high *melt projection area* during
510 periods of low-flow is comparable to that produced at other times, but there is much less of the
511 low *melt projection area* material. Assuming, as seems reasonable that high area is associated
512 with fine particles, this will shift the mean of the PSD towards smaller values. Moreover, this
513 pattern does not appear to be confined to the extreme excursions highlighted in **Figures 11-13**.
514 With reference to **Figure 10** we can see that even during periods of ‘normal’ operation,
515 significantly less low area material is present when the flow is lower (**Figure 10b**) relative to
516 when the melt flow is higher (**Figure 10a**).

517

518 **5 Summary and Conclusions**

519 We have shown how relatively inexpensive consumer DSLR equipment can provide useful
520 complimentary data to the more commonly reported high speed imaging experiments for
521 monitoring the melt plume during close-coupled gas atomization. Using only the ratios of the
522 signals in the R, G and B channels, the colour information within the image can be used to
523 obtain spatially resolved, semi-quantitative temperature maps of the melt plume, akin to the
524 traditional foundry technique of using colour charts to gauge temperature. By utilising the
525 absolute intensity data recorded by the CCD we can then also estimate the *relative melt*
526 *projection area* responsible for the optical emission, allowing a spatially resolved estimate of
527 the location of melt break-up within the atomization plume to be made. As far as we are aware
528 this is the first time such a determination of the location of break-up within a melt plume has
529 been made directly. As such, the system offers a potentially exciting means to evaluate the
530 performance of atomizer design modification *in situ*, using relatively low cost equipment. The
531 value of the analysis is not so much in being able to predict the PSD of the final powder product,
532 which require a much more complex analysis than that offered here, but rather to visualise
533 where finely divided material (and hence break-up) is located within an atomization plume.

534

535 **Acknowledgements**

536 This work was funded by MAPP – The EPSRC Future Manufacturing Hub in Manufacture
537 using Advanced Powder Process (Grant No. EP/P006566/1). Photography was by Tom
538 Williamson at Atomising Systems Ltd., Sheffield.

539

540

541

542 **References**

- 543 Achelis, L., Uhlenwinkel, V., Lagutkin, S. and Sheikhaliev, S., Atomization using a pressure-gas-
544 atomizer, in *Progress in powder metallurgy, parts 1 & 2* (eds. D.Y. Yoon, S.J.L Kang, K.Y Eun &
545 Y.SKim), *Mater. Sci. Forum*, vol. **534-536**, pp. 13-16, 2007.
- 546 Anderson, I.E. <https://www.youtube.com/watch?v=BgiwGmf4fFc>. Video of the initial stages of gas
547 atomization of stainless steel, Ames Laboratory, Iowa, USA, 2011.
- 548 Anderson, I.E., Achelis, L., Two Fluid Atomization Fundamentals, In: Henein, H., Uhlenwinkel, V.,
549 Fritsching, U. (eds) *Metal Sprays and Spray Deposition*. Springer, Cham.
550 https://doi.org/10.1007/978-3-319-52689-8_3, 2017.
- 551 Aphale, S. S., DesJardin, P. E., Development of a non-intrusive radiative heat flux measurement for
552 upward flame spread using DSLR camera based two-color pyrometry, *Combust. Flame*, vol. **210**
553 pp. 262–278, 2019.
- 554 Arachchilage, K.H., Haghshenas, M., Park, S., Zhou, L., Sohn, Y., McWilliams, B., Cho, K., Kumar,
555 R., Numerical simulation of high-pressure gas atomization of two-phase flow: Effect of gas pressure
556 on droplet size distribution. *Adv. Powder Technol.*, vol. **30**, pp. 2726-2732, 2019.
- 557 Bigg, T.D. and Mullis, A.M., Spatially resolved velocity mapping of the melt plume during high
558 pressure gas atomisation of liquid metals, *Metall. Mater. Trans. B*, vol. **51**, no. 5, pp. 1973-1988,
559 2020.
- 560 Felice, R.A. and Nash, D.A, Pyrometry of materials with changing, spectrally-dependent emissivity -
561 Solid and liquid metals, *AIP Conf. Proc.* vol. **552**, pp. 734–739, 2013.
- 562 Fiorentina, P., Bertolo, A., Cavazzani, S., Ortolani, S., Calibration of digital compact cameras for sky
563 quality measures, *J. Quant. Spectrosc. Radiat. Transf.*, vol. **255**, pp. 107235, 2020.
- 564 Hsiang, L.-P. and Faeth, G.M., Near-limit drop deformation and secondary breakup. *Int. J. Multiphase*
565 *Flow*, vol. **18**, pp. 635-652, 1992.
- 566 Jimenez, S., Two-color, two-dimensional pyrometers based on monochrome and color cameras for
567 high-temperature (1000 K) planar measurements, *Rev. Sci. Instrum.* vol. **91**, pp. 114901, 2020.

568 Kaiser, R., Li, C., Yang, S. & Lee, D., A numerical simulation study of the path-resolved breakup
569 behaviors of molten metal in high-pressure gas atomization: With emphasis on the role of shock
570 waves in the gas/molten metal interaction. *Adv. Powder Technol.*, vol. **29**, pp. 623-630, 2018.

571 Kuhn, P. B., Ma, B., Connelly, B. C., Smooke, M. D., Long, M. B., Soot and thin-filament pyrometry
572 using a color digital camera, *Proc. Combust. Inst.* vol. **33**, pp. 743–750, 2011.

573 Larciprete, M.C., Gloy, Y.S., Li Voti, R., Cesarini, G., Leahu, G., Bertolotti, M. and Sibilica, C.,
574 Temperature dependent emissivity of different stainless steel textiles in the infrared range, *Int. J.*
575 *Thermal Sci.*, vol. **113**, pp. 130-135, 2017.

576 Li, X-g. and Fritsching, U., Process modeling pressure-swirl-gas-atomisation for metal powder
577 production, *J. Mater. Process. Technol.*, vol. **239**, pp. 1-17, 2017.

578 Mates, S.P. and Settles, G.S., A study of liquid metal atomization using close-coupled nozzles, Part 1:
579 Gas dynamic behavior, *At. Sprays*, vol. **15**, no. 1, pp. 19-40, 2005.

580 Motaman S., Mullis A.M., Cochrane R.F. & Borman D.J., Numerical and experimental
581 investigation of the effect of melt delivery nozzle design on the open- to closed-wake
582 transition in closed-coupled gas atomization. *Metall. Mater. Trans. B*, vol. **46**, pp. 1990-
583 2004, 2015.

584 Mullis, A.M., Adkins, N.E., Aslam, Z., McCarthy, I.N. and Cochrane, R.F., High frame rate analysis
585 of the spray cone geometry during close-coupled gas atomization, *Int. J. Powder Metall.*, vol. **44**,
586 no. 1, pp. 55-64, 2008.

587 Mullis, A.M. Ashok-Kuma, A.P. and Borman D.J., CFD modelling of high pressure gas atomization of
588 liquid metals, in *CFD Modelling and Simulation of Materials Processing 2018* (eds. Nastac, L.,
589 Pericleous, K., Sabau, A., Zhang, L., Thomas, B.), The Minerals, Metals & Materials Series.
590 Springer, Cham. https://doi.org/10.1007/978-3-319-72059-3_8.

591 Mullis, A.M., McCarthy, I.N. and Cochrane R. F., High speed imaging of the flow during close-coupled
592 gas atomisation: Effect of melt delivery nozzle geometry, *J. Mater. Process. Technol.*, vol. **211**, no.
593 9, pp. 1471-1477, 2011.

594 Mullis, A.M., McCarthy, I.N., Cochrane, R.F. and Adkins, N.J., Log-Normal Melt Pulsation in Close-
595 Coupled Gas Atomization, *Metall. Mater. Trans. B*, vol. **44**, no. 4, pp. 789-793, 2013.

596 Mullis, A.M. and Dunkley, J.J., Analysis of acoustic emissions from gas atomization, in *Proc. of*
597 *PowderMet 2016 (Advances in Powder Metallurgy and Particulate Materials 2016)*, 5-8 June 2016,
598 Boston MA, Metal Powder Industries Federation. ISBN 978-1-943694-11-2, 2016a.

599 Mullis, A.M. and Dunkley, J.J., Analysis of acoustic emissions from gas atomization, in *Proc. World*
600 *PM Congress 2016*, 9-13 October June 2016, Hamburg, Germany, 2016b.

601 Mullis A.M., Farrell, L., Cochrane R. F. & Adkins N. J., Estimation of cooling rates during close-
602 coupled gas atomization using secondary dendrite arm spacing measurement, *Metall. Mater. Trans.*
603 *B*, vol. **44**, pp. 992-999, 2013.

604 Mullis, A.M., Jegede, O.E., Bigg, T.D., & Cochrane R.F., Dynamics of core-shell particle formation in
605 drop-tube processed metastable monotectic alloys, *Acta Mater*, vol. **188**, pp. 591-598, 2020.

606 Neumann, S., Dubberstein, T., Chaves, H., Kirmse, C. and Schwarze, R., Influencing parameter study
607 on primary breakup of free falling steel melt jets using volume of fluid simulation, *Steel Res. Int.*,
608 vol. **87**, no. 8, pp. 1002-1013, 2016.

609 Sievers, A.J, Temperature dependence of the emissivity of transition metals, *Solar Energy Mater.*, vol.
610 **1**, pp. 431-439, 1979.

611 Sankaranarayanan, A., Swami, U., Sasidharakurup, R., Chowdhury, A., Kumbhakarna, N.,
612 Investigation of sooting flames by color-ratio pyrometry with a consumer-grade DSLR camera, *Rev.*
613 *Sci. Instrum.*, vol. **92**, pp. 044905, 2021.

614 Thompson, J.S., Hassan, O., Rolland, S.A. & Sienz, J., The identification of an accurate simulation
615 approach to predict the effect of operational parameters on the particle size distribution (PSD) of
616 powders produced by an industrial close-coupled gas atomiser. *Powder Technol.*, vol. **291**, pp. 75-
617 85, 2016.

618 Ting, J. and Anderson, I.E., Computational fluid dynamics investigation of wake closure phenomena,
619 *Mater. Sci. Eng. A*, vol. **379**, no. 1-2, pp. 264-276, 2004.

620 Ting, J., Connor, J. and Ridder, S., High-speed cinematography of gas-metal atomization, *Mater. Sci.*
621 *Eng. A*, vol. **390** no. 1-2, pp. 452-460, 2005.

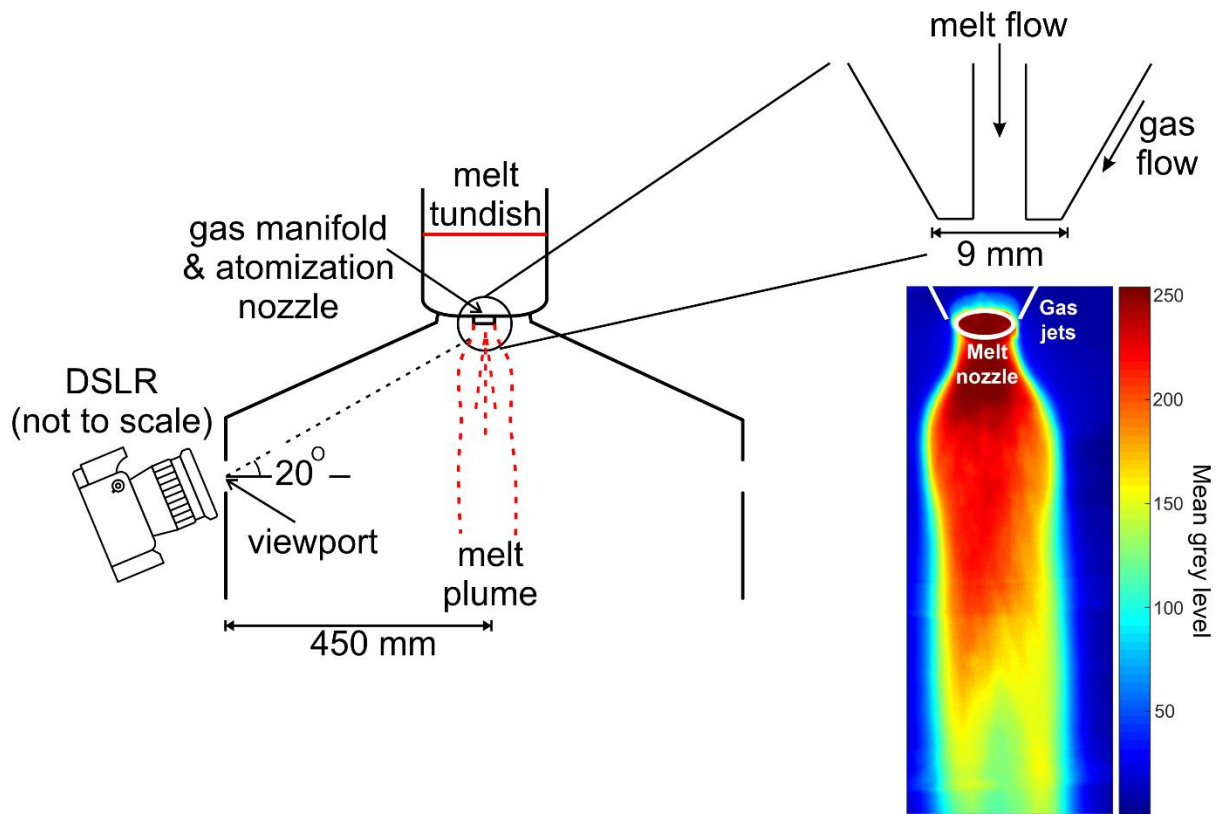
622 Ting, J., Peretti, M.W. and Eisen, W.B., The effect of wake-closure phenomenon on gas atomization performance,
623 *Mater. Sci. Eng. A*, vol. **326**, no. 1, pp. 110-121, 2002.

624 Xu, L., Zhou, X., Li, J., Hu, Y., Qi, H., Wen, W., Du, K., Ma, Y. & Yu, Y., Numerical Simulations of
625 Molten Breakup Behaviors of a de Laval-Type Nozzle, and the Effects of Atomization Parameters
626 on Particle Size Distribution. *Processes*, vol. **8**, pp. 1027, 2020.

627 Zeoli, N., Tabbara, H. and Gu, S., Three-dimensional simulation of primary break-up in a close-coupled
628 atomiser, *Appl. Phys. A*, vol. **108**, no. 4, pp. 783-792, 2012.

629 Zhou, C., Wang, S., Cao, Y., Yang, S-H, Bai, B., Online pyrometry calibration for industrial combustion
630 process monitoring, *Processes*, vol. **10**, pp. 1694, 2022.

631



632

633

Figure 1. Schematic diagram showing orientation of camera to the atomization

634

system and close-up of the melt nozzle & gas manifold. Supersonic gas flow is

635

delivered from an annular slit type nozzle (a concentric opening located at the top of

636

the melt nozzle, with the outer surface of the melt nozzle forming the inner surface of

637

the gas annulus). The melt plume shape is shown schematically and is based upon

638

that determined by Mullis *et al.* (2018).

639

640

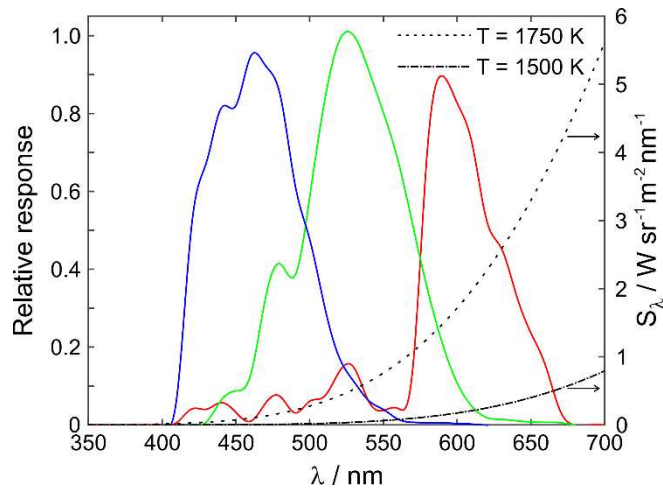


641

642 **Figure 2.** Typical DLSR image of the gas atomisation of 316L stainless steel. Also
 643 shown, towards the top of the image, is the window used to optically measure the melt
 644 flow used in the generation of **Figure 7**, and for temperature calibration against the
 645 melt tundish thermocouple.

646

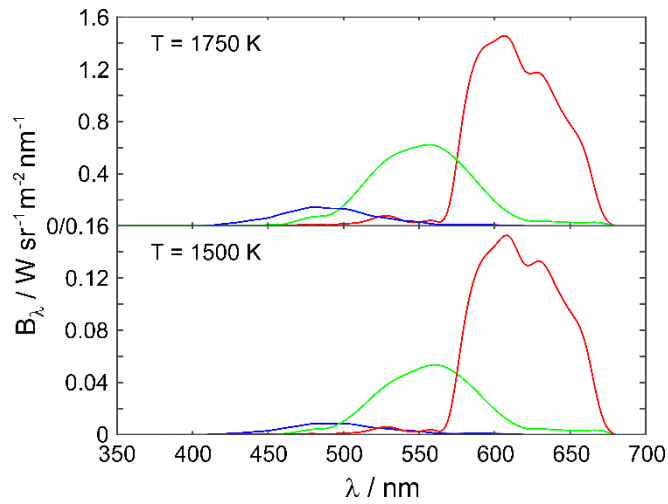
647



648

649 **Figure 3.** Relative RGB response of the Nikon CCD used to obtain the colour image
 650 shown in **Figure 2**. Also shown are calculated blackbody curves for material at $T =$
 651 1500 K and $T = 1750 \text{ K}$ (right hand axis).

652



653

654

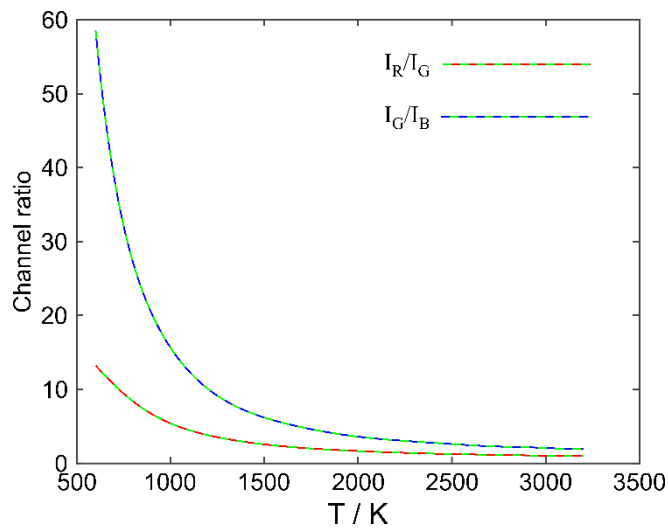
Figure 4. Relative power in the R, G, B channels of the camera CCD as a function of object temperature, T , for a blackbody source. Note that scales for $T = 1500$ K and $T = 1750$ K differ by one order of magnitude.

655

656

657

658



659

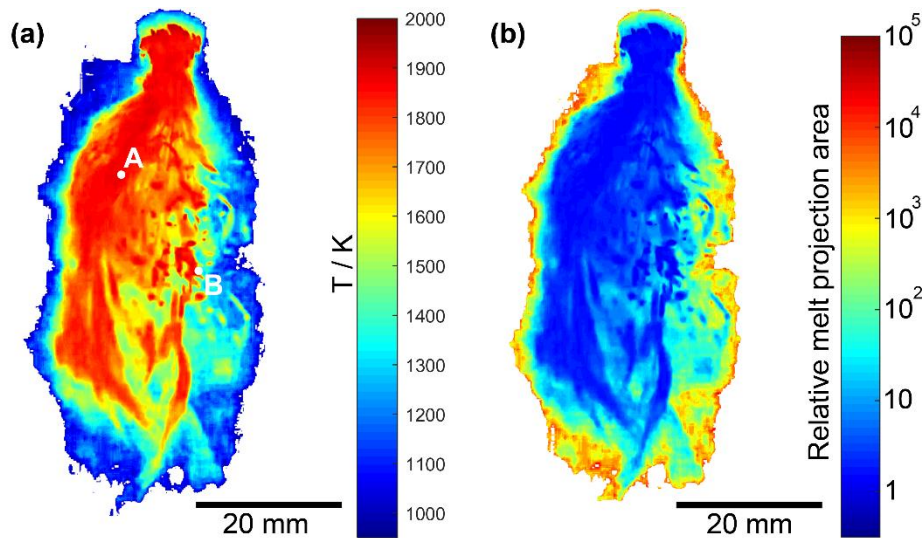
660

Figure 5. Ratio of colour response I_R/I_G and I_G/I_B as a function of blackbody temperature for the camera used to obtain **Figure 2**.

661

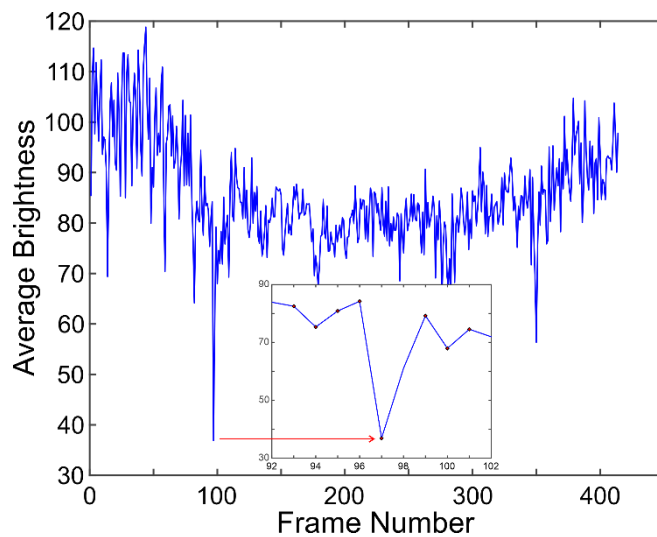
662

663



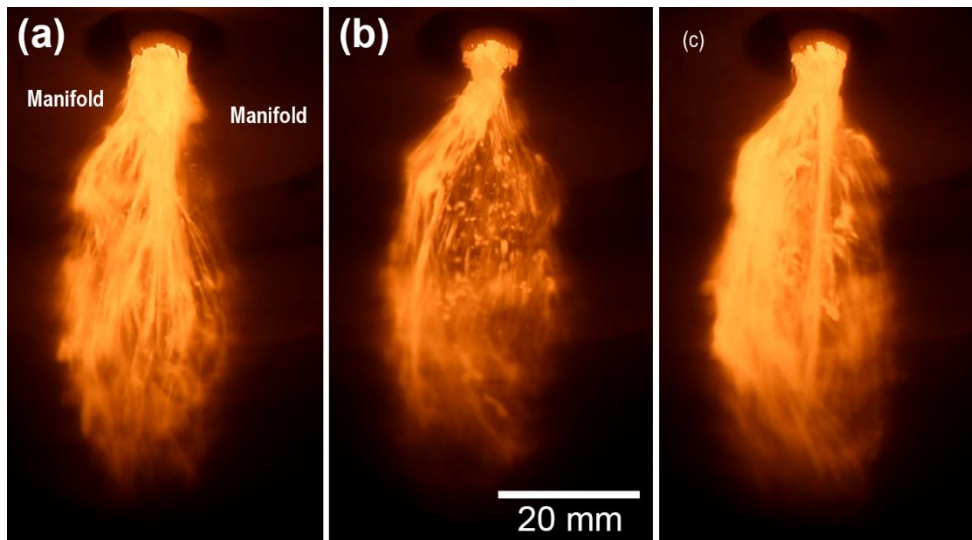
664

665 **Figure 6.** (a) Estimated temperature map based on colour channel ratios for the
 666 atomization plume shown in Figure 1 and (b) the *relative melt projection area*,
 667 calculated on the basis of the absolute intensity in the green channel for material at the
 668 local temperature shown in part (a). The locations marked “A” and “B” in part (a) of
 669 the figure indicate typical regions of minimum and maximum temperature gradients
 670 respectively.



671

672 **Figure 7.** Typical intensity in each frame of the movie calculated by sampling a narrow
 673 window, 5 pixels high, placed immediately below the melt outlet nozzle. Insert shows
 674 detail of an extreme low intensity excursion identified in frame 97.



675

676 **Figure 8.** Three frames from the movie depicting typical operation of the gas atomizer.

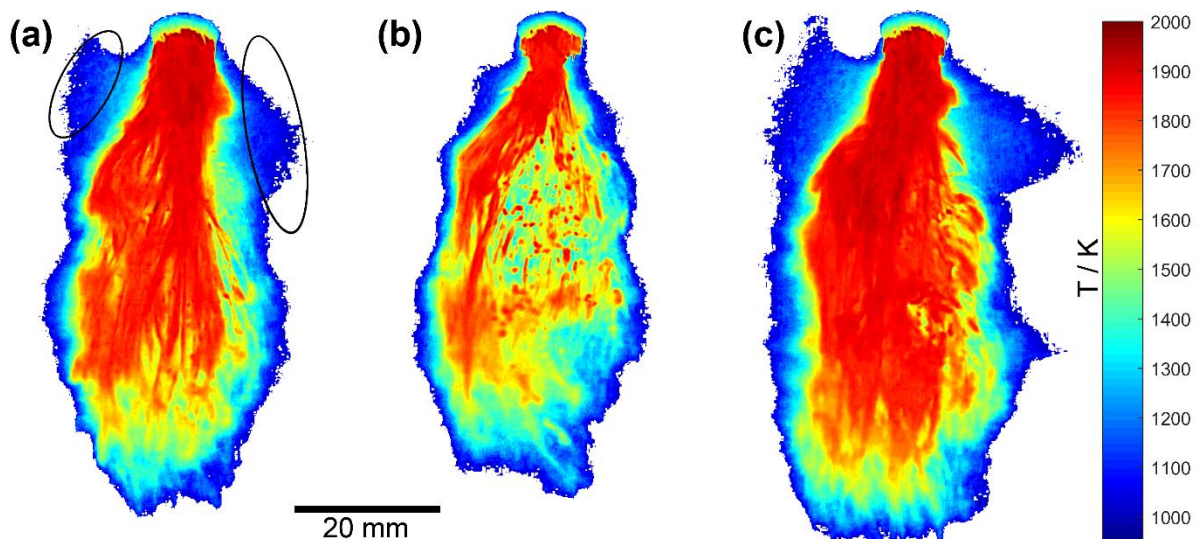
677 (a) frame 44, brightest mean intensity; (b) frame 243 typical of low mean intensity (c)

678 frame 269, mean intensity close to its time-averaged global value. The portion of the

679 gas manifold behind the melt plume is visible in most frames in reflected light as a dull

680 red ring and is labelled in part (a) of the figure.

681

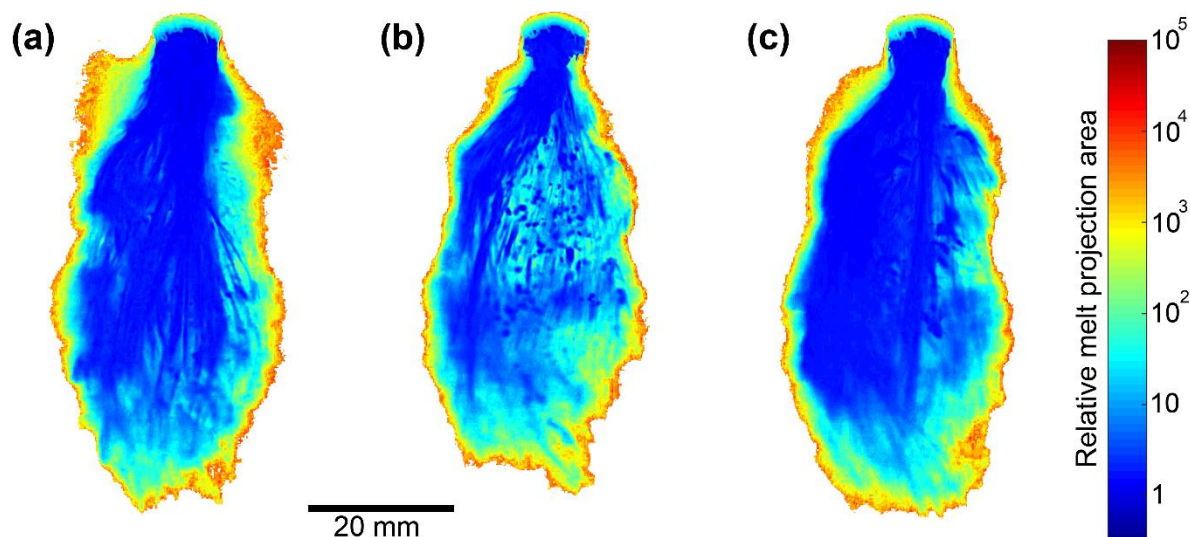


682

683 **Figure 9.** Temperature maps corresponding to the three images shown in **Figure 8**. A

684 temperature artefact arising from reflection off the gas manifold is visible in some

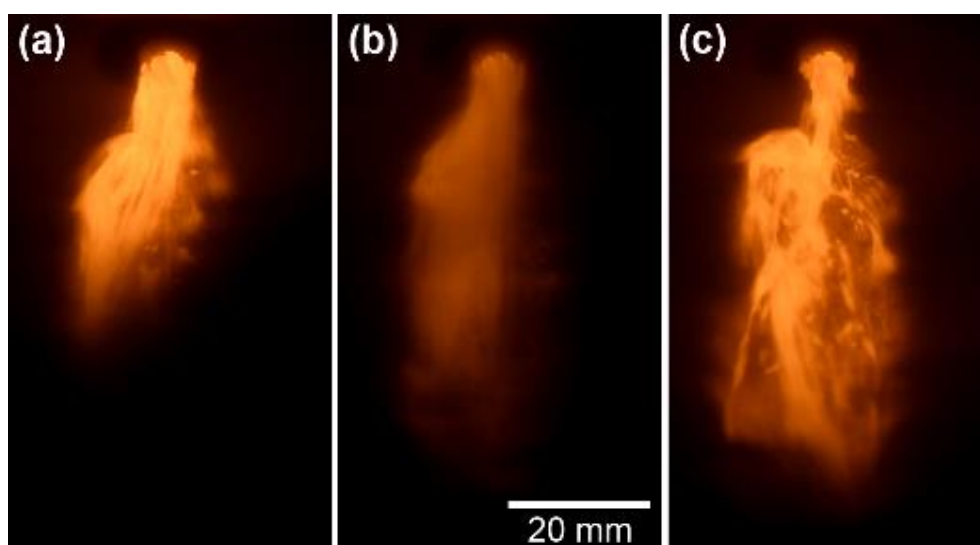
685 frames and has been highlighted by two black ellipses in part (a) of the figure.



686

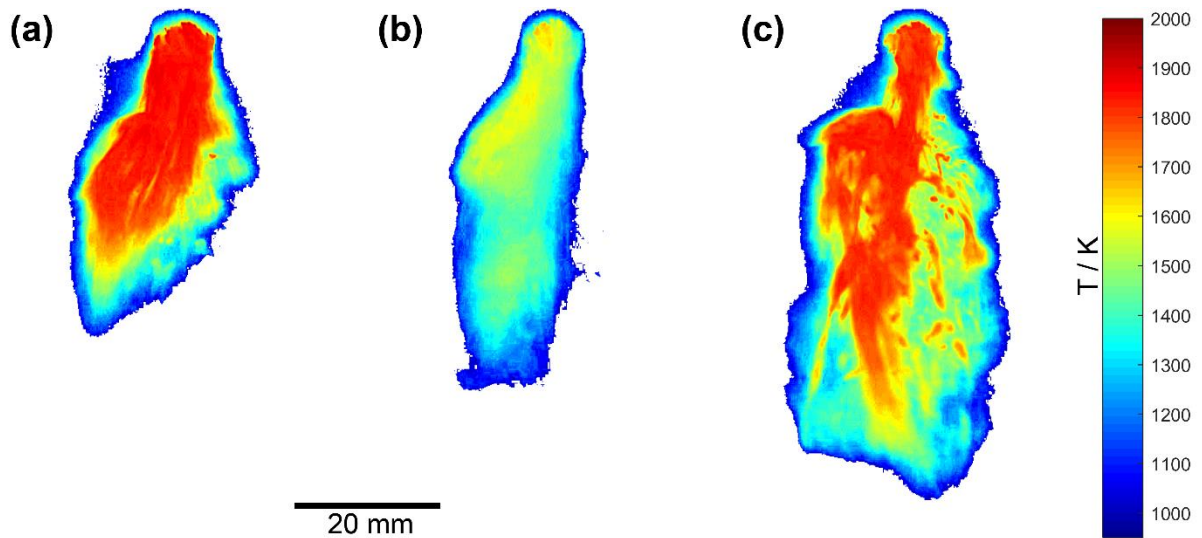
687 **Figure 10.** Maps of *relative melt projection area* corresponding to the three images
 688 shown in **Figure 8**.

689



690

691 **Figure 11.** Three frames from the movie illustrating an extreme low intensity
 692 excursion by the atomizer in which melt delivery is close to being shut-down. (a)
 693 Frame 96, immediately prior to the melt shut-down, (b) frame 97 during near melt
 694 shut-sown and (c) frame 98 atomizer recovering normal operation. Note the
 695 morphology of the melt in part (c) which is similar to membrane break-up observed at
 696 the start of atomization.

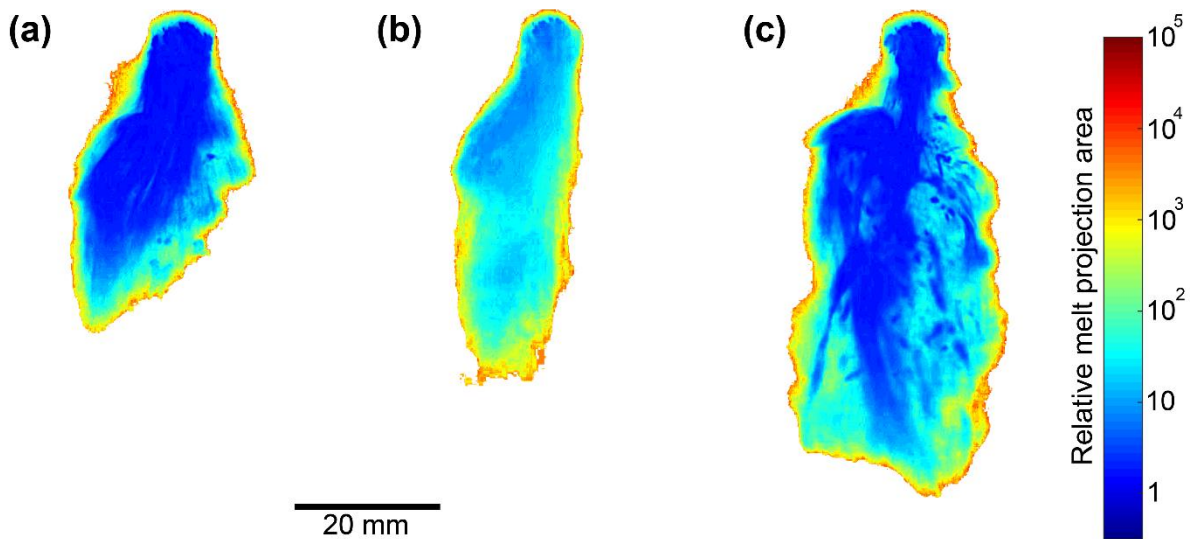


697

698 **Figure 12.** Temperature maps corresponding to the three images shown in **Figure 11**.

699

700



701

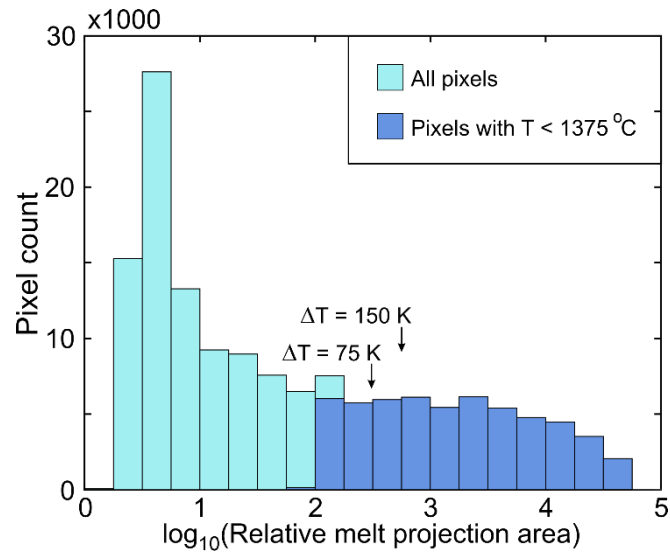
702 **Figure 13.** Maps of *relative melt projection area* corresponding to the three images
 703 shown in **Figure 11**.

704

705

706

707



708

709 **Figure 14.** Histogram showing distribution of \log_{10} of the *relative melt projection area* (based
 710 upon pixel count), extracted from **Figure 6b**. Also shown are those pixel that contain material
 711 below the liquidus temperature of the atomized material (correlating with data from Figure 6a),
 712 wherein the material would be solid on the assumption of 0 undercooling for nucleation. We
 713 also give an indication of how far to the right the solid/liquid transition would move for an
 714 assumed nucleation undercooling of 75 K and 150 K.